CrystEngComm

Accepted Manuscript

ROYAL SOCIETY OF CHEMISTRY

www.rsc.org/crystengcomm

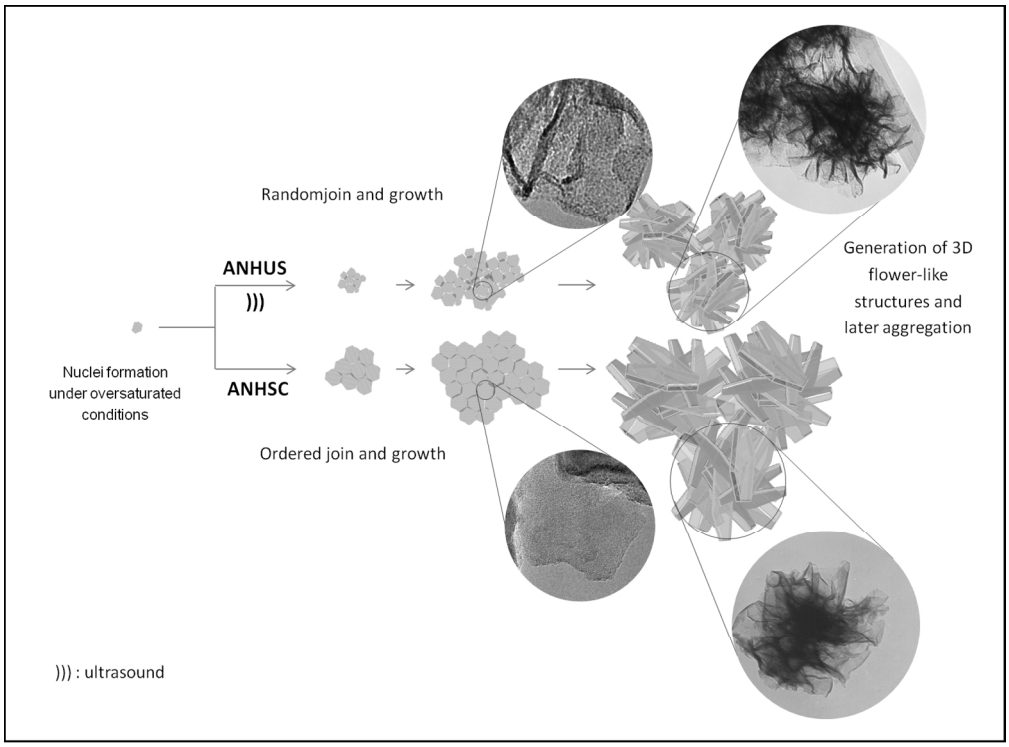

265x195mm (150 x 150 DPI)

Influence of ultrasound in the instantaneous synthesis of tridimensional α-$Ni(OH)_2$ nanostructures and derived NiO nanoparticles.

S. Cabanas-Polo[a]*, Z. Gonzalez[a], A. J. Sánchez-Herencia[a] and B. Ferrari[a]

[a] Instituto de Cerámica y Vidrio, CSIC. c/Kelsen, 5. 28049 Madrid, Spain

* Corresponding author.

Abstract

Nickel hydroxides present an extraordinary importance in the development of electrochemical devices. In contrast to the use of ammonia as a direct precipitating agent, we present herein the instantaneous precipitation of α-$Ni(OH)_2$ nanopowders by the addition of a nickel salt to an ammonia solution. The synthesis is based on the oversaturation of the solution in the absence of any additive or other metallic cations where the ammonia plays a role as a complex agent for intermediate nickel compounds. The influence of the ultrasound in both the micro- and the crystalline structure is discussed and the differences are referred to a new parameter (S parameter) which quantifies the number of watts per cm^2 that a mol of $[Ni(NH_3)_6]^{2+}$ experiences. The description of the nucleation and growth processes of the different powders studied led to the understanding of the effect of ultrasound in the crystallography of α-$Ni(OH)_2$. Porosity of the samples is also evaluated and its percentage and type is also correlated to the synthesis conditions. The transformation of α-$Ni(OH)_2$ to NiO is also considered and their optical properties are evaluated as an initial indicator of their promising used as electrochemical devices.

Introduction

The coexistence of mobile and immobile ionic components in electrochemical devices requires mechanical durability and structural stability in order to preserve its functionality. In this sense the employment of nanostructured compounds, whose interface effects play a crucial role on the overall ionic/electronic transport properties, requires of nanostructured arrangements that preserve the stability while providing a high surface area that accelerate the reactions [1,2]. Consequently the 3D nanostructured materials, such as dendritic structures, nanopillers and/or nanoflowers, have attracted considerable attention due to their large surface area [3]. Nickel hydroxide has been extensively studied over the last few decades as the positive electrode of alkaline rechargeable batteries (Ni-Cd, Ni-MH and Ni-H_2) and/or as a common precursor of nickel and nickel oxide for catalytic devices and ceramic industry or for gas sensing applications [4–10]. For this reason its synthesis as complex and stable nanostructures focuses on the influence of the morphology and crystallography of the synthetic nickel hydroxide particles on its electrochemical activity. Some recent papers have proved that the decrease of crystallite size and the increase of structural defects (turbostraticity, cations vacancies and/or stacking faults) improve the electrochemical activity of this material [11,12]. Moreover, 0D, 1D, 2D and 3D morphologies have been compared, resulting in a higher electrochemical activity and superior cycling reversibility of the 3D hierarchical nanostructures [11–18]. Some other characteristics of 3D hierarchical nanostructures of nickel based compounds are now on focus due to the chemical and magnetic activity of metallic nickel [19].

Nickel hydroxide crystallizes in two different polymorphs, α- and β-$Ni(OH)_2$. Both are laminar hydroxides being β-$Ni(OH)_2$ the stable phase which crystallizes in an hexagonal crystallographic structure isostructural with brucite, where each nickel atom is coordinated to six hydroxyl groups creating an octahedron. These octahedrons share their vertexes to create a laminar structure. On the other hand, α-$Ni(OH)_2$ is a metaestable phase due to a lack of hydroxyl groups within its structure that force foreign anions to be intercalated within the nickel-hydroxyl layers to maintain its electroneutrality, leading it to a hydrotalcite-like structure [20–22]. The crystallographic structure of this metaestable phase is not well describe, since the interlaminar space depends on the type of inclusion present in the structure, which normally varies from 7 to 8 Å [23,24]. The presence of these anions, along with water molecules within the structure, results in a turbostratic phase whose basal planes are not perfectly aligned along the c axis but slightly deviated from one another. Pure α-$Ni(OH)_2$ is unstable and transforms to the beta polymorph during synthesis or in strong alkali media [25]. The electrochemical activity of nickel hydroxide is affected by the different crystallographic structure of the polymorphs. This

way, the oxidized form achieved with the alpha phase (γ-NiOOH) presents a theoretical specific capacity of 433 mAh/g, while the oxidized form of the beta phase (β-NiOOH) only reaches 289 mAh/g [13]. Moreover, the alpha phase also exhibits a high ionic exchange capacity and electrocatalytic activity [24,26]. Many attempts have been made to stabilize this metaestable phase. In this sense, the addition of some metallic cations seems to increase the stability of α-$Ni(OH)_2$ by the incorporation of new structural defects and the employment of different synthesis additives seems to retain the alpha structure preventing it to transform into the beta one [15,23,27,28].

Sonochemistry has been employed successfully for the synthesis of nickel hydroxide nanopowders in the last years [21,27,29]. The crystallization under the effect of ultrasound has been studied showing that nucleation of solid crystals is affected by the presence of ultrasonic waves. Ultrasound can induce primary nucleation in particle-free solutions at lower supersaturation levels [30]. Another effect of the ultrasound on nucleation is shortening the induction time between the establishment of supersaturation and the onset of nucleation and crystallization [31]. All these effects have been observed in sulfates and oxides where it has been proved that the ultrasound has an effect on nucleation resulting in finer and more uniform crystals. This has been justified on the segregation in a liquid mixture by pressure gradients induced by the cavitation bubbles [32].

In this work, the instantaneous precipitation of α-$Ni(OH)_2$ nanopowders from an ammonia solution with a nickel salt is presented. In contrast to previous synthesis, ammonia is not used as a direct precipitating agent or as a liquid medium [23,27] but as an intermediate complex agent for nickel ions previous to precipitation of nickel hydroxide. Ultrasound is applied to the reaction to study its effect on the crystal structure of the fabricated powders.

Results and discussion

Influence of ultrasound in the morphology of the α-$Ni(OH)_2$

Previous results showed that the conditions for the synthesis of nickel hydroxide powders can be established through the study of the predominant species diagram as a function of pH and log [Ni^{2+}] for a fixed ammonia concentration of 2.0 M. When the Ni^{2+} concentration is 0.1 M, the synthesis proceeds by the complexion of Ni^{2+} to create $[Ni(NH_3)_6]^{2+}$, which provides a characteristic blue color to the solution. In these conditions, under the effects of ultrasound, the ammonia concentration decreases by a degassing process reducing the pH of the solution

and leading to the precipitation of β-$Ni(OH)_2$ powders [22]. The general scheme for these reactions is as follows:

$$Ni^{2+} + 6NH_3 \rightarrow [Ni(NH_3)_6]^{2+}$$

$$[Ni(NH_3)_6]^{2+} + 2OH^- +))) \rightarrow Ni(OH)_2 + 6NH_3\uparrow$$

However, when the concentration of Ni^{2+} is 0.65 M, oversaturation conditions are reached and the complex ion $[Ni(NH_3)_6]^{2+}$ immediately transforms into a light green powder of α-$Ni(OH)_2$ (sample ANHSC) following:

$$Ni^{2+} + 6NH_3 \rightarrow ([Ni(NH_3)_6]^{2+})^* \rightarrow Ni(OH)_2$$

In the instantaneous synthesis of α-$Ni(OH)_2$, no ammonia is released to the atmosphere and the complex ion $[Ni(NH_3)_6]^{2+}$ is just a short life intermediate. Macroscopically, the presence of ultrasound does not alter the instantaneous precipitation behavior and a similar powder is obtained.

Several syntheses were performed under the influence of ultrasound changing the ultrasonic power and the precursor volume (powders ANHUS-1 to ANHUS-6), and the influence of the sonocrystallization on the resulting nanostructure was firstly evaluated. In order to correlate the results between different samples obtained under different experimental conditions, we propose a parameter called "S parameter" which measures the sonication effectiveness, which is equivalent to the number of watts per cm^2 (given by the ultrasonic horn and calculated by a calorimetric method) that a mol of $[Ni(NH_3)_6]^{2+}$ experiences (calculated from the ammonia concentration considering the stoichiometric ratio between Ni^{2+} and NH_3). Three volumes of precursors (50, 80 and 200 ml) were used as well as two ultrasonic powers (45 and 80 W/cm^2). That means, the S parameter ranged from 0 $W/cm^2 \cdot mol$ for the synthesis developed under silence conditions (ANHSC), to 4000 $W/cm^2 \cdot mol$ (table 1).

The XRD plots in figure 1 shows that all the as-synthesized powders (both under silence conditions or in the presence of ultrasound) correspond to the alpha polymorph of nickel hydroxide, except sample ANHUS-6 where a mixture of both α- and β-$Ni(OH)_2$ was obtained. The presence of the β-$Ni(OH)_2$ phase in the product of the ANHUS-6 synthesis is due to the higher volume of precursors tested (200 ml). Powder filtration process takes place under basic conditions (10<pH<12), so the larger the volume, the longer is the filtration process which favors the transformation of the alpha polymorph into the beta one [21]. The density of all these samples (from ANHUS-1 to ANHUS-5), determined by He picnometry, was found to be in the

range 2.7-2.9 g/cm^3, which represents 65-70% of the theoretical density of the stable beta phase (4.10 g/cm^3).

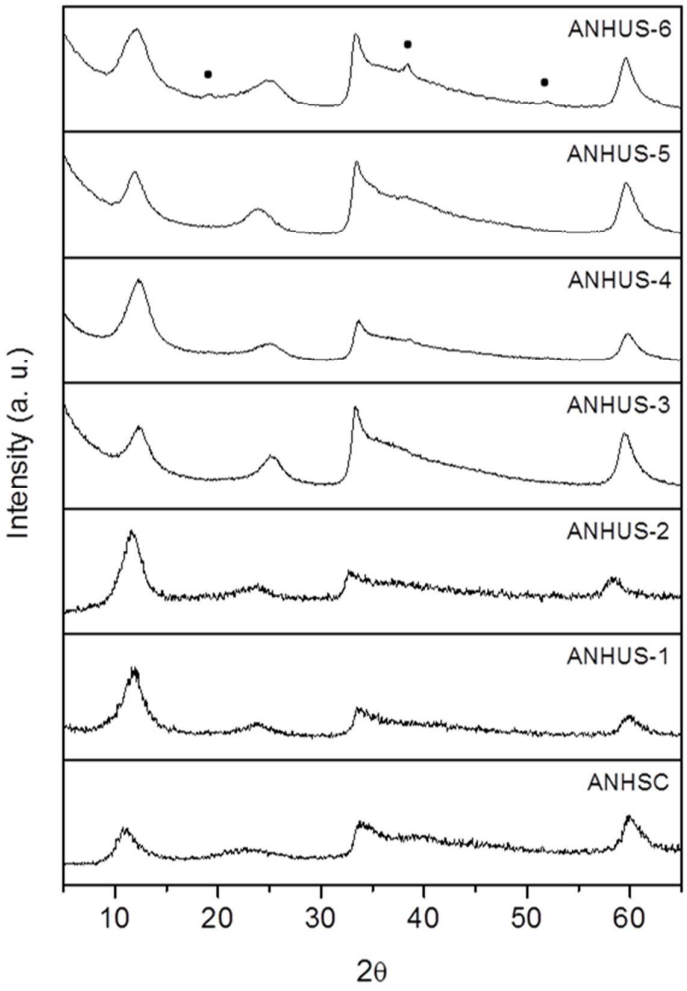

Fig. 1. XRD plots of samples prepare under different conditions (shown in table 1). All peaks correspond to α-Ni(OH)$_2$ except the ones pointed with (•) in sample ANHUS-6 that correspond to β-Ni(OH)$_2$.

Figure 2 shows FE-SEM micrographs of all the powders synthesized: sample ANHSC (fig. 2a), prepared under silence conditions, where S = 0 W/cm^2·mol, samples ANHUS-6 and ANHUS-5 (figs. 2b and 2c, respectively), prepared using a sonication power of 45 W/cm^2 and different volumes of precursor, and samples ANHUS-3, ANHUS-2 and ANHUS-1 (figs. 2d, 2e and 2f, respectively), prepared using a sonication power of 80 W/cm^2 and different volumes of precursors.

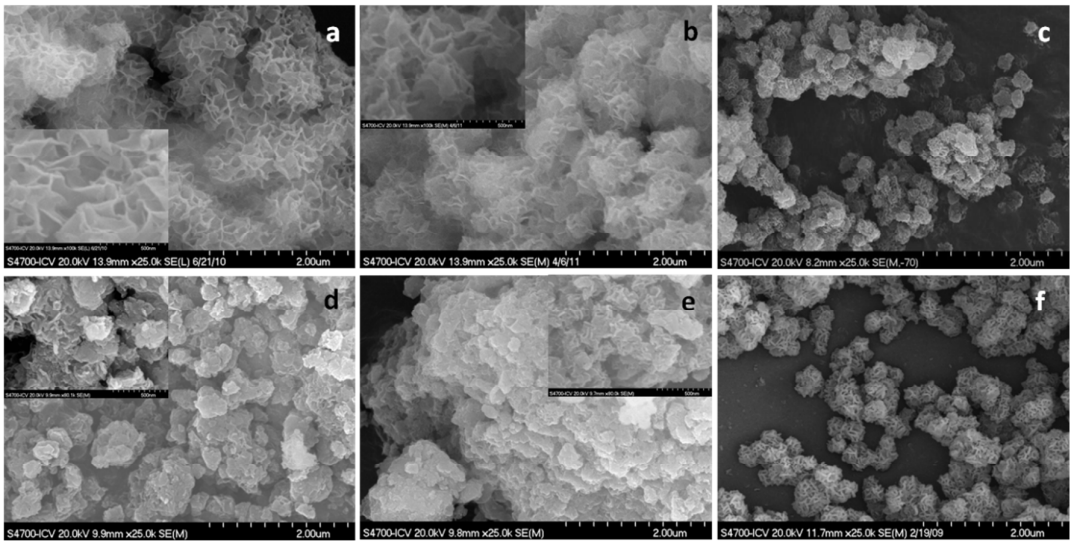

Figure 2. FESEM images of a) sample ANHSC where a spongy 3D flower-like structure with wall thickness <20 nm can be observed, b) ANHUS-6, c) ANHUS-5, d)ANHUS-3, e) ANHUS-2 and f) ANHUS-1.

As it is observed for sample ANHSC (fig. 2a), a 3D spongy aggregate is obtained when a sheet of α-$Ni(OH)_2$ is folded in on itself. This conformation can be understood by picturing a piece of paper slightly wrinkled. As it is observed, ANHSC powder presents a 3D flower-like morphology, where an irregular three-dimensional surface in an apparently continuous structure is created. The inset at higher magnification reveals that the thickness of the walls that conforms the spongy-like aggregates (nanopetals of the flower-like structures) is < 20 nm.

Sample ANHUS-6 (fig. 2b), prepared after applying 45 W/cm^2 to a large volume of precursor (200 ml) shows a similar morphology of that of sample ANHSC. However, when the initial volume decreases (sample ANHUS-5, 80 ml), individual and isolated α-$Ni(OH)_2$ flower-like particles, with sizes in the range 300-400 nm, are obtained (fig. 2c). For S parameter values below 700 W/cm^2 mol (sample ANHUS-6), the α-$Ni(OH)_2$ phase still precipitates instantaneously forming a similar 3D flower-like nanostructure than in the case of silence conditions. However, the same sonication power (45 W/cm^2) applied to a lower volume of precursors (sample ANHUS-5, S = 1500 W/cm^2 mol) promotes a better dispersion of nuclei that individually and instantaneously precipitate forming small and discrete flower-like nanostructures when growing.

When the sonication power is increased to 80 W/cm^2 and similar volumes are employed (200, 80 and 50 ml for samples ANHUS-3, ANHUS-2 and ANHUS-1, respectively), different structures are observed. On the one hand, a clear breakdown of the flower-like continuous structure that

was obtained in samples ANHSC and ANHUS-6, can be perceived for the larger volumes of precursors tested, where the sonication effectiveness is 1200 W/cm^2 (fig. 2d, sample ANHUS-3, 200 ml) and 3000 W/cm^2 (fig. 2e, sample ANHUS-2, 80 ml). Although the floral morphology can still be appreciated (insets of figures 2d and 2e), it is not longer so evident at the whole powder inspection. However, independent flower-like 3D nanostructures reappear for 50 ml of solution (fig. 2f, sample ANHUS-1) where sonication effectiveness achieves 4000 W/cm^2 mol. A larger reaction volume implies a higher number of nuclei that can be originated, which favors the overlapping between nucleation and growth processes. Although the ultrasound itself promotes the dispersion of the nuclei once they are formed, the Oswalt ripening growth mechanism promotes the incorporation of the newly formed nuclei into the growing particles and, as a result, a semi-continuous irregular structure without floral morphology is obtained. Nevertheless, when the volume of the starting solution is decreased to 50 ml, a lower nucleation rate is achieved. The nuclei are dispersed by the effect of the ultrasound and no overlapping with the growing step is observed, what leads to the obtaining of 3D flower-like nanostructures. It is then worth noting that, if isolated α-Ni(OH)$_2$ flower-like nanostructures are to be obtained, the higher the sonication power applied to the starting solution, the higher should be the S parameter in order to separate nucleation and growth process.

Table 1 summarizes the main morphological characteristics of the powders produced with and without sonication. In agreement with the results showed above, the synthesis conditions are ordered attending to the level of sonication applied during the synthesis: SC, 45 and 80 W/cm^2. The table collects main morphological characteristic of as-synthetized powders determined by N_2 adsorption/desorption, such as the modified BET specific surface area (SSA) and the total pore volume, obtained from the N_2 adsorption isotherm, as well as the open SSA and the micropore volume determined by the t-plot method. Differences in SSA and pore volume values can be correlated to the SSA and volume associated with the micropores (pores less than 2 nm diameter), since the "open SSA" obtained from the t-plot currently provides the SSA from mesopores, macropores and external surface. Therefore, contributions of the micropores to the particle morphology are also collected in the table as a percentage of the BET parameter.

Table 1. Synthesis conditions (ultrasonic power, volume of precursors and S parameter), SSA characteristics (BET SSA, OPEN SSA and % SSA contributed by micropores), porosity, and crystallographic parameters (interlaminar distance and crystal size) of synthetic powder.

	ANHSC	ANHUS-6	ANHUS-5	ANHUS-3	ANHUS-2	ANHUS-1

Ultrasonic power (W/cm^2)	-	45	45	80	80	80
Volume (ml)	50	200	80	200	80	50
S parameter ($W/cm^2 \cdot mol\ [Ni(NH_3)_6]^{2+}$)	0	670	1500	1200	3000	4000
BET SSA (m^2/g)	49.5	-	39.9	13.8	6.6	69.9
Open SSA by t-plot (m^2/g)	45.04	-	37.1	12.7	4.8	65.9
% SSA contributed by micropores	9%	-	7%	7%	27%	6%
Total Pore Volume N_2 (cm^3/g)	0.305	-	0.205	0.089	0.031	0.300
Micropore Volume by t-plot (cm^3/g)	0.002	-	0.001	0.000	0.000	0.001
% Micropore on N_2 pore volume	0.6%	-	0.5%	0.0%	0.0%	0.3%
Interplanar distance c (Å±0.2)	7.9	-	7.1	7.2	7.4	7.5
Crystal size L_{klm} (nm±0.3)	4.0	-	2.4	3.7	4.0	2.2

The analysis of the data in table 1 shows that there are not significant differences in the SSA calculated by the BET and t-plot methods, except in the case of ANHUS-2, where the contribution of micropores to the total SSA is 27%. However, the evaluation of the N_2 pore volume evidences that ANHUS-2 and ANHUS-3 show no or negligible micropore volume. The micropore contributions (% Micropore on N_2 pore volume) in ANHSC, ANHUS-1 and ANHUS-5 powder are below 1% of the total pore volume and do not overpass the 10% of the total exposed surface (% SSA contributed by micropores). Then, it can be concluded that microporosity in α-$Ni(OH)_2$ powders synthesized by the instantaneous precipitation, with or without sonication, is not relevant if compare with the contribution of macroporosity, mesoporosity and the external surface. The evaluation of the SSA values also evidences that the disappearance of the flower-like nanostructure in the ANHUS-2 and the ANHUS-3 powders dramatically decreases the SSA, specifically in the case of ANHUS-2, where the total SSA fall down to 6.6 m^2/g. The external specific surface area of the flower-like particles (Open SSA calculated by t-plot) ranges from 37 to 66 m^2/g and it can be correlated with the measurement of the irregular surface of the 3D nanostructure.

Figure 3 shows the adsorption/desorption isotherms of N_2 at liquid N_2 temperature and the pore size distribution of the as-synthesized ANHSC, ANHUS-1 and ANHUS-5 powders (fig. 3a), as well as a detail of the nanostructure of the petals in the flower-like 3D nanostructure of ANHUS-1 and ANHUS-5 powders (figs. 3b and 3c, respectively).

Shapes of the isotherms indicate a marked difference among powders while the low adsorbed volume at very low relative pressure ($P/P_o < 0.01$) verifies the short amount of micropores within the flower-like particles. The type II nitrogen isotherm of the ANHUS-5 evidences the macroporous structure of the flower-like powders. The hysteresis is very narrow indicating the presence of fine macropores. On the other hand, samples ANHSC and ANHUS-1 show a significant hysteresis pattern but not a plateau at high P/P_o like the Type IV isotherms. Such isotherm shape indicates that the material contains both mesopores (responsible for the hysteresis) and macropores resulting from the absence of a plateau and the steep slopes in relative pressure range of 0.98-1.00. The ANHUS-1 and ANHSC isotherms also show the forced closure of the desorption branch at $0.4 < P/P_o < 0.5$ evidencing the presence of small mesopores with diameters < 4 nm, extended up to 10 nm for ANHUS-1. The large volume uptake at P/P_o near 1.0 showed by ANHSC and ANHUS-1 indicates the presence of porosity over the 100 nm range. The pore size distributions plotted as a function of the adsorbed volume of N_2 are showed in the inset of figure 3a. Distributions quantify differences in mesoporosity and macroporosity among powders. For the ANHUS-5 powder the distribution is bimodal with a major peak between 20-60 nm and a minor and smooth peak at 2-3 nm. ANHSC distribution shows a similar trend, with a higher peak (a higher amount of adsorbed gas) between 30-70 nm and a similar minor peak, while the ANHUS-1 nanostructures exhibit a quasi-unimodal distribution with an intense peak ranging 30-70 nm similar to ANHSC and a wide population of small mesopores ranging from 3 to 10 nm.

The analysis of the porosity of resulting aggregates from the ANHSC, ANHUS-1 and ANHUS-5 synthesis suggests the presence of a multiscale pore structure which corresponds to the 3D nanostructure morphology of the flower-like α-$Ni(OH)_2$ particles. Fine mesopores correspond to the spaces left by the staking of the α-$Ni(OH)_2$ turbostractic units. In this sense, the small mesopores (< 4 nm) of ANHSC and ANHUS-5 correspond to the absence of sonication or a mild sonication, respectively, while the wideness of the mesopore range (3-10 nm) in ANHUS-1 evidences the strong effect of the S parameter and/or the mechanical disruption in the stacking of the α-$Ni(OH)_2$ units during growing. The large mesopores and fine macropores can be related to the porosity within aggregates, i. e. the porosity generated among petals when the flower-like nanostructure grows. Similar pore size distributions for samples ANHSC and ANHUS-1 in this range (20-100 nm) is in good agreement with the similitude between features of particles shaped by the aggregation of petals or platelets with thicknesses below 20 nm, that can be observed in the inset of figure 2a (ANHSC) and the image in figure 3b (ANHUS-1). Also a lower volume of narrower pores (20-60 nm) in the ANHUS-5 nanostructure matches

with the detail of the 3D structure showed in figure 3c. This flower-like particles exhibit small petals and a less intricate structure which results in a more open and less active surface.

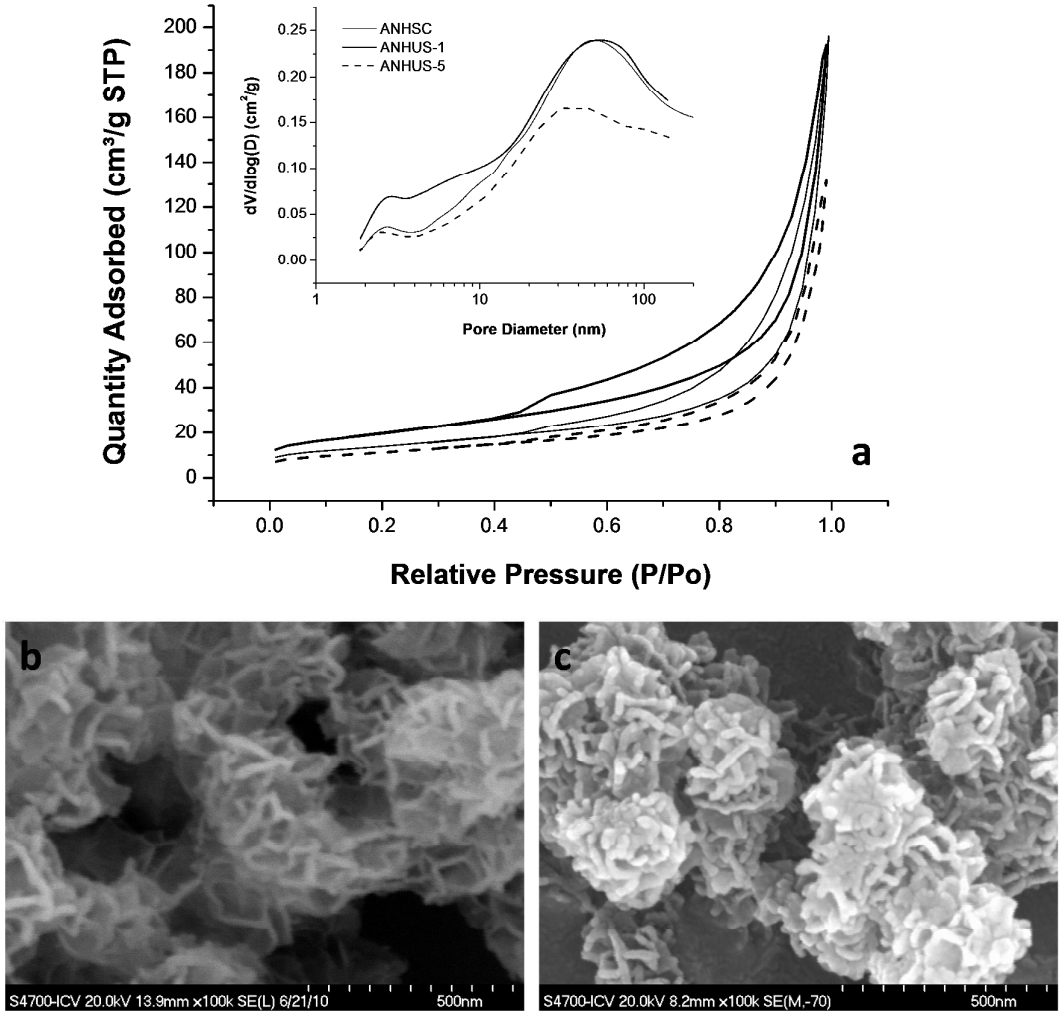

Figure 3. a) Adsorption-desorption isotherms of N_2 and the partial volume of each pore diameter measured for ANHSC, ANHUS-1 and ANHUS-5. Micrographs of the petal structure of b) ANHUS-1 and c) ANHUS-5 powders.

Based on the previous observation on how the sonication power and the S parameter affect the powder morphology, two different samples, ANHUS-1 and ANHUS-5, were chosen to study their particle size and colloidal stability. After the total removal of the unreacted precursors, the powders were dispersed in deionized water at pH 9 (adjusted with HTMA) to simulate the pH condition of the post-reaction media. The zeta potential values of as-synthesized flower-like nanostructures were found to be +66 ± 3 mV for ANHUS-1 and +17 ± 6 mV for ANHUS-5, in

agreement with Open SSA data in table 1. Under these conditions the particle size distribution was determined for both powders by DLS. Results are shown in figure 4 where the particle size distributions in both number (figure 4a) and volume (figure 4b) fractions for ANHUS-1 and ANHUS-5 powders are plotted. From the plots related to the left axis, the particle size distribution in number approaches that in volume for both powders, which means that the particles in suspension have reached their maximum dispersion [22]. The mean particle size of ANHUS-1 is 190 nm in number and 295 nm in volume, while the mean values of the population ANHUS-5 nanostructures are 530 nm and 615 nm in number and volume, respectively. Those values are in good agreement with the aggregate sizes observed in the FE-SEM micrographs (Figures 2c and 2f). Moreover, powders exhibit particle distributions slightly biased to the left, evidencing the natural and spontaneous growth of 3D nanostructures and identifying the smaller particles obtained from each synthesis: D_{V10} is 170 for ANHUS-1 and 370 for ANHUS-5.

In this sense, the number and volume fractions corresponding to the 10%, 50% and 90% of the population of the 3D nanostructures can be extracted from accumulative data (the plots related to the right axis). Those values and sizes as well as sizes determined by SEM inspection are collected in table 2 as well as the BET diameter (D_{BET}), calculated from SSA and particle density, and the agglomeration factor (F_{ag}) [22]. All these parameters were related to the sonication conditions. Data determine that the size of 3D nanostructures produced under mild sonication conditions (ANHUS-5, 1500 W/cm^2·mol $[Ni(NH_3)_6]^{2+}$) ranges from 370-955 nm, while those produced under extreme sonication (ANHUS-1, 4000 W/cm^2·mol $[Ni(NH_3)_6]^{2+}$) ranges from 170-425 nm. In any case, both powders are well-dispersed and stable in the post-reaction medium. Consequently, the increase of sonication effectiveness leads to a smaller and more homogeneous population of flower-like nanostructures. Mesoporosity and particle size of nano-flowers support the mechanism of reaction proposed from microscopy data. When individual 3D nanostructures grow under the effect of ultrasound, the higher is the sonication power the more disordered and delicate is the nanostructure. The higher applied S parameter (4000 W/cm^2·mol) leads to intricate 3D nanostructures, with a narrower particle size distribution (170-425 nm), thinner walls (< 20nm), larger open SSA (65.9 m^2/g, and larger meso-macroporosity, 20-100 nm) and more disordered lattice stacking (larger mesoporosity, 3-10 nm).

Table 2. Main parameters of the particle size distributions determined by DLS and particle sizes determined by SEM for ANHUS-1 and ANHUS-5 nanostructures

		ANHUS-5	ANHUS-1
Ultrasonic power (W/cm^2)		45	80
Volume (ml)		80	50
S parameter ($W/cm^2 \cdot mol\ [Ni(NH_3)_6]^{2+}$)		1500	4000
Mean Particle Size in number (nm)		530	190
Particle Size Distribution Values	D_{V10} (nm)	370	170
	D_{V50} (nm)	615	295
	D_{V90} (nm)	955	425
D_{BET} (nm)		555	317
F_{ag}		~1	~1
D_{SEM} (nm)		>300	<300

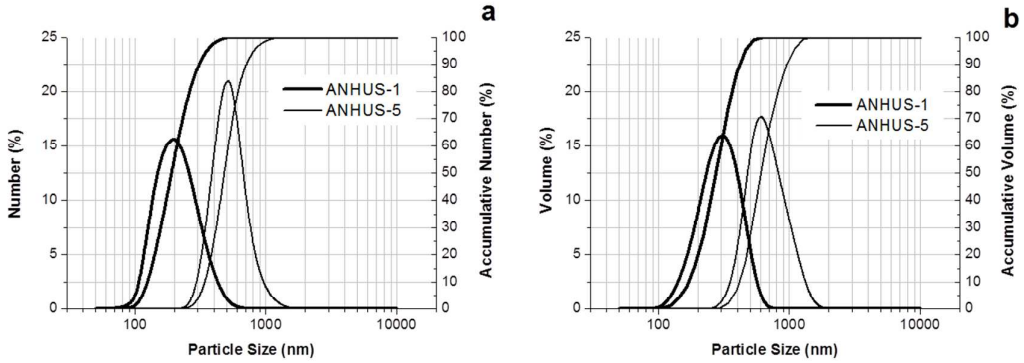

Figure 4. Particle size distribution of samples ANHUS-1 and ANHUS-5 at the post-reaction conditions in number (a) and volume (b).

Influence of ultrasound in the crystallography of the α-Ni(OH)$_2$

The evolution of particle size agrees with the SAA values determined by N_2 adsorption/desorption. Moreover, the porosity analysis suggests that the ultrasound not only affects the dispersion of nuclei and the subsequent particle size and specific surfaces, but also the morphology of the nanostructure and the distribution of the porosity at the whole nanostructure, signifying that it could have a strong effect at all levels of growing and structural, and even of crystallographic ordering.

According to the Warren modification of Scherrer formula and using the peak position and the full width at half maximum (FWHM) of (001) reflection, in the XRD plots, the crystallite size was calculated [33]. Table 1 shows also the crystallographic parameters of the powders obtained under sonication compared with those produced in silence conditions. The interlaminar distances were calculated from the XRD plots in figure 1, except sample ANHUS-6 where a mixture of both α- and β-$Ni(OH)_2$ was obtained. As it is observed, the sonicated powders present lower values of interlaminar distance and crystal size if compare to ANHSC sample. Among sonicated powders, the influence of both volume and ultrasonic power over the crystallographic parameters follows a similar trend. For example, for a fixed volume of 80 ml and increasing sonication power (ANHUS-5 and ANHUS-2), the higher the S parameter, the larger is the interplanar distance and the crystal sizes. At the same time, when the ultrasonic power is kept constant and the volume increases (samples ANHUS-2 and ANHUS-3), the same trend is observed, i. e. the lower the S parameter, the smaller is the interplanar distance and the crystal size. Moreover, flower-like nanostructures, both ANHUS-5 and ANHUS-1, present a significant decrease of the crystal size, although the interplanar distance remains in the range of the other particles synthetized under ultrasound.

In order to further investigate the effect of ultrasound in the crystallographic characteristics of the instantaneously synthesized flower-like particles, a constant volume of 50 ml of the starting solution was considered, i. e. ANHSC and ANHUS-1 synthesis. Figure 5 (a and b) shows the TEM micrographs of samples ANHUS-1 and ANHSC, respectively. These images evidence the decreases in size of the 3D nanostructures produced by the ultrasound, since ANHSC doubles in size the ANHUS-1 particles. Besides the size, no other significant differences can be observed at this magnification. However, the HRTEM micrographs of samples ANHUS-1 and ANHSC (fig. 5c and 5d) do show differences in the 2D structures of the particles, i. e. in the nanopetals of the 3D flower-like particles. In the case of sample ANHSC (fig. 5d) a homogeneous α-$Ni(OH)_2$ sheet is observed while in the case of ANHUS-1 (fig. 5c) different crystalline domains (little spots) can be distinguished within the 2D nanostructure which can actually be intuited at low magnification in the TEM micrograph of figure 5a. In figure 5c (powders ANHUS-1) these different randomly ordered crystalline domains can be clearly observed.

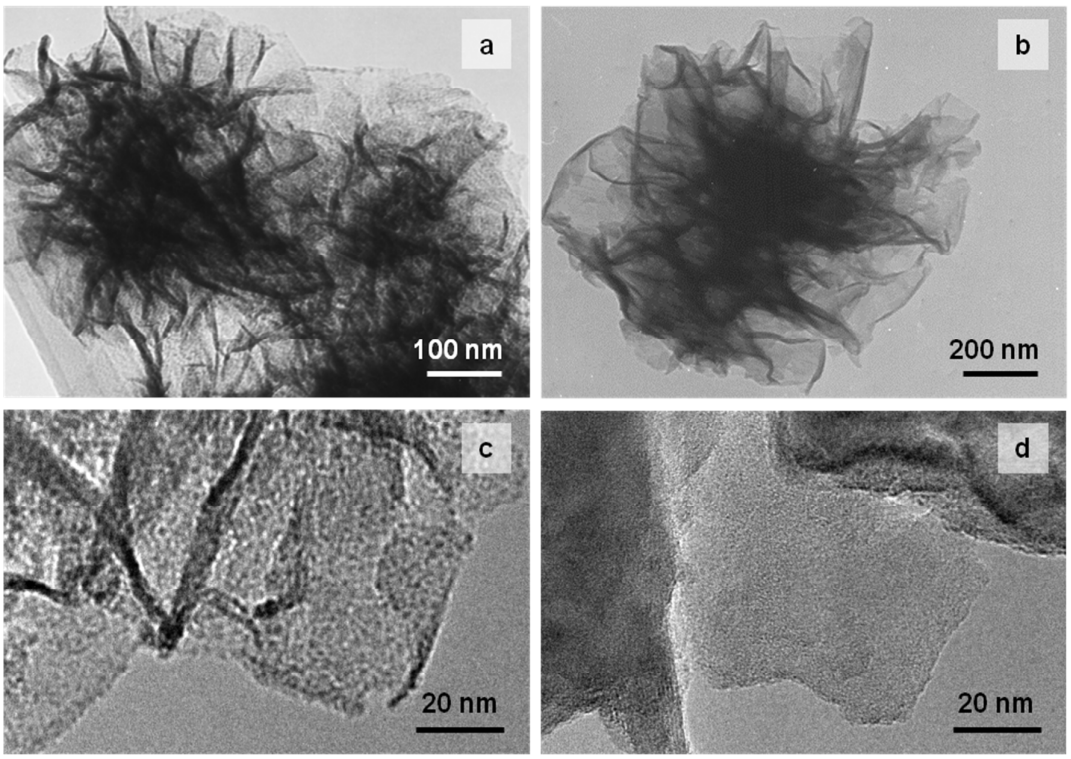

Figure 5. TEM (a and b) and HRTEM (c and d) images of samples ANHUS-1 (a and c) and ANHSC (b and d).

Figure 6 shows three HRTEM micrographs at higher magnifications of sample ANHUS-1 (a and c) and sample ANHSC (b). Differences in crystal size of alpha nickel hydroxide can be observed in figure 6 (a and b). During the microscopic analysis and due to beam irradiation, the powder evolves and suffers a dehydration process and a new re-crystallization to produce NiO (fig. 6c). The inset figures on figure 6c, show interplanar distances of 2.4 Å that correspond to the (101) planes of the NiO. Figure 6a shows the ANHUS-1 structure at the beginning of the dehydration process and fig 6c shows the same region after the re-crystallization process. Although the $Ni(OH)_2$ has transformed to NiO, figure 6c allows us to clearly observe that the crystallite size in ANHUS-1 is around 2.2 nm, which agrees with that calculated from the X-ray diffractogram of sample ANHUS-1 using the Warren modification of Scherrer formula.

The unique conditions reached with ultrasound, specially the high pressures and cooling rates, also generates a series of distortions within the reaction media that reduce the mobility of the growing crystallites leading them to a spatial confinement [34,35]. In these sense, when two growing nuclei approach, the mechanical disruption nullify their ability to couple and naturally grow, confining the crystals (0D structures) in a 2D nanostructured aggregate during the

ultrasonicated synthesis [29,36]. This default in the growth ordering is also the origin of the presence of a large population of fine mesopores in ANHUS-1 (figure 3a and 5c). In contrast, for powder ANHSC (Figure 5d) the absence of the mechanical disruption allows the growing crystals to minimize their surface energy by aligning in the (00l) plane in the 2D continue structure. During growth, the altered crystal orientation in sonicated powders promotes a spatial confinement leading to smaller crystal domains.

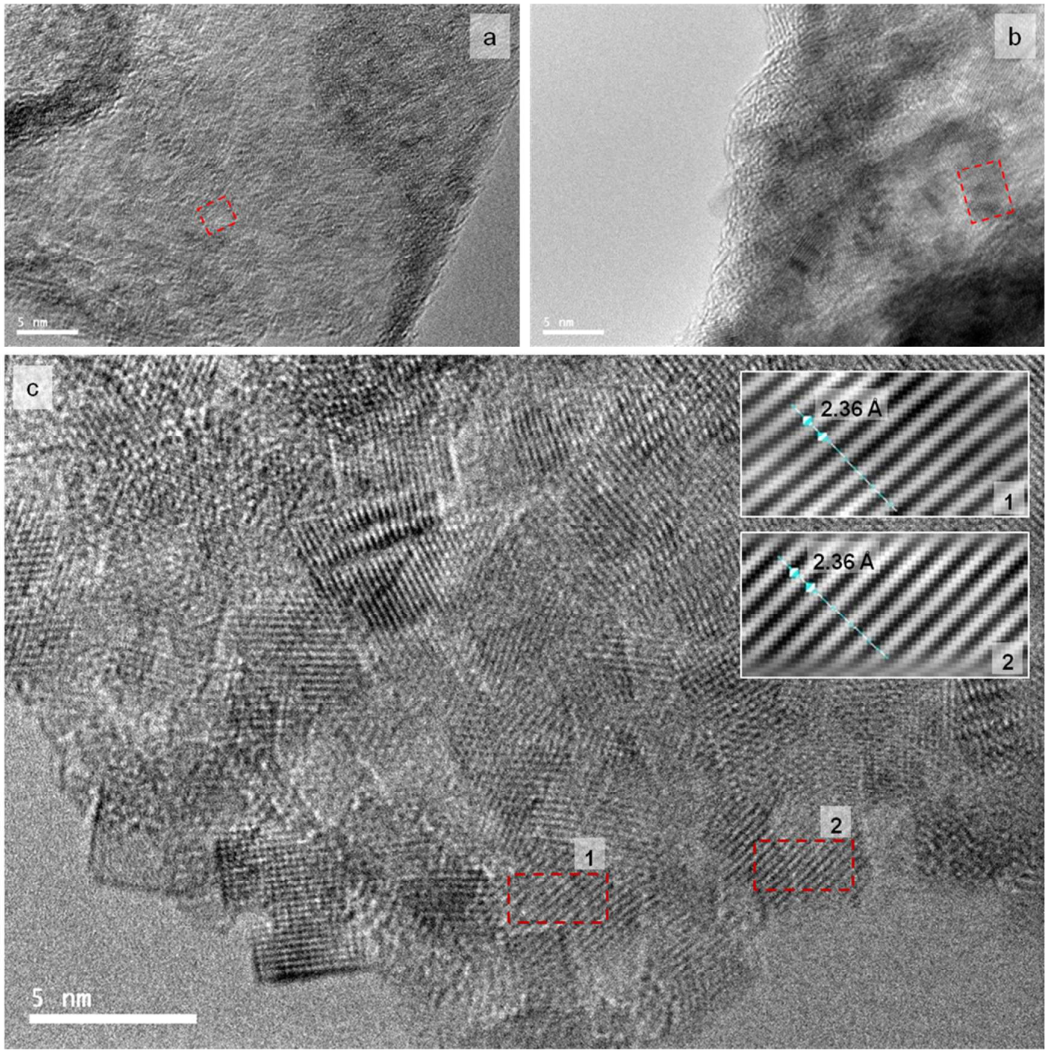

Figure 6. HRTEM images of sample a) ANHUS, b) ANHSC (where the different crystallite sizes can be observed) and c) NiO, derived from the transformation of $Ni(OH)_2$ due to the analysis conditions. After transforming to NiO, crystallographic distances along the (101) plane of NiO

can be observed (inset figures in figure 6c).

Figure 7a shows in detail the powder XRD pattern of sample ANHUS-1, which exhibits wide and irregular peaks as expected from the particle sizes in the nanoscale range. As it was explained above, both ANHSC and ANHUS-1 powders were identified as the turbostratic α-$Ni(OH)_2$ phase (Figure 7a) characterized by an asymmetric peak at approximately d = 2.66 Å (110 plane) [21,25]. One may observe that both patterns present the same reflections (indexed using the JCPDS card 22-0444) but it should be noted that peaks non-related to the c-axis, i.e. (110) and (300), appear at approximately the same diffraction angle for both powders while peaks related to the c-axis, i.e. (001) and (002), present significant deviations between them. Deviations in the diffraction angle of peaks related to the c-axis are due to variations in the interlaminar space. In our particular case, these values, calculated directly from the XRD graphs, are 7.5 Å and 7.9 Å for samples prepared with and without ultrasound, respectively. Furthermore, in all our experiments, the interlaminar distance for samples prepare with ultrasound never overcome 7.5 Å while in the case of samples prepare in absence of ultrasound the values are always higher. The presence of curve lines in the (001) plane direction (instead of straight ones) in the HRTEM micrograph of sample ANHUS-1 (fig. 7b) could be due to the interaction of two different crystal as well as to the presence of a stacking faults, which would be in agreement with the previously exposed results.

A detailed study in HRTEM (Figure 7c and 7d) approaches the thickness of the 2D nanopetals (10-20 nm) that conformed ANHUS-1 and ANHSC nanostructures with their corresponding IFFT analysis and the distances in the (001) plane. According to these images, the interlaminar distances in the (001) direction are 6.6 Å and 9.8 Å for samples ANHUS-1 and ANHSC, respectively, and these distances are constant through at least six planes in each sample. It can be clearly noticed that these values differ from those calculated from the XRD data due to the diffractograms irregularity and the lattice relaxation of the isolated particles which can be inspected by HRTEM. However, interlaminar values follow a similar trend being lower than those of the sonicated powder.

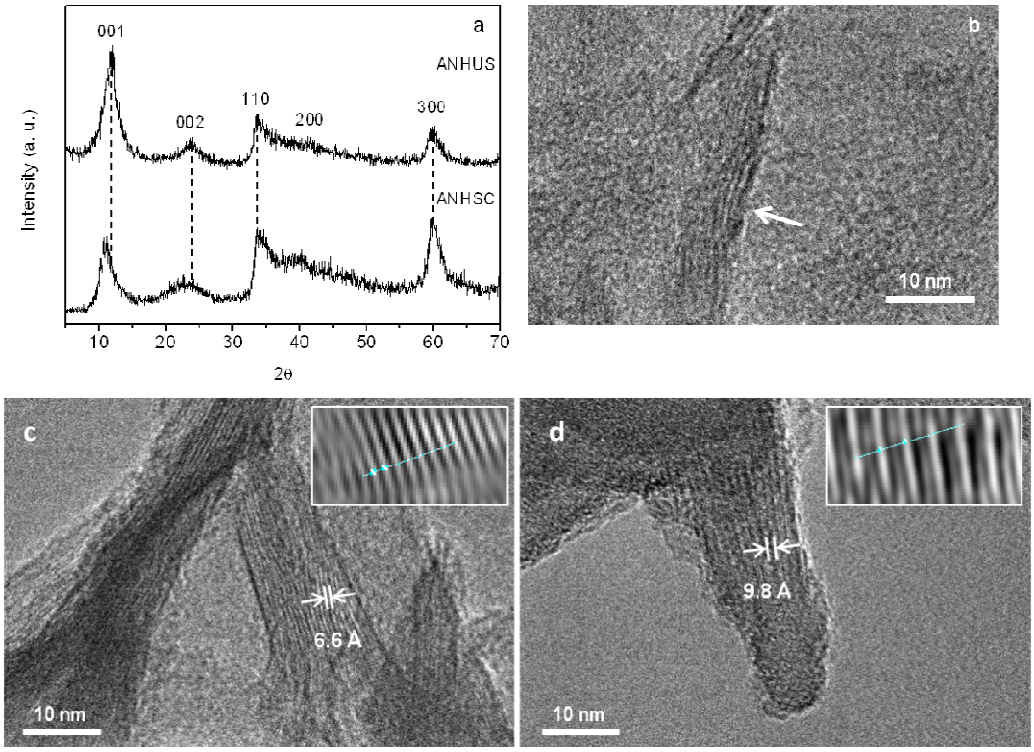

Figure 7. a) XRD pattern of samples ANHUS-1 (above) and ANHSC (below), identified as the α-$Ni(OH)_2$ using the JCPDS card 22-0444, b) HRTEM image of sample ANHUS-1 showing stacking faults along the 001 plane, c and d) HRTEM micrographs of ANHUS-1 and ANHSC with its corresponding IFFT, respectively.

In order to evaluate the origin of the differences in the interlaminar space determined by XRD and HRTEM between particles obtained under sonicated and silence conditions, the thermal behavior of both powders was investigated. As it can be observed in the DSC-TGA measurements of figure 8 (a and b), both powders present a wide asymmetric peak between room temperature and 240 °C approximately that corresponds to superficially physisorbed and interlamellar water losses. The mass loss for this phenomenon was close to 7 % of the total one in the case of ANHUS-1 nanostructure (fig. 8a) and 10 % in the case of ANHSC (fig. 8b). The smaller amount of water content in the case of the nano-flower synthesized with the aid of ultrasound is due to the smaller interlaminar distance, as seen by XRD, achieved in this powder as a consequence of the sonication. The second peak of DSC curve, centered at approximately 280 °C, corresponds to the transformation of $Ni(OH)_2$ to NiO ($Ni(OH)_2 \rightarrow NiO + H_2O$). For ANHUS-1, this process presents a mass loss of near 17 %, quite close to the 19 % theoretical value, and for ANHSC the loss is about 15 %. Finally, a small peak centered at approximately

350 °C with an associated mass loss of approximately 5 % is observed for both powders. In order to determine the origin of this last peak, FTIR measurements of the gases generated at that temperature during the DSC-TGA experiments were carried out. The FTIR spectrum of sample ANHUS-1 (inset graph in fig. 8a) shows two sharp peaks at 1632 and 1597 cm^{-1} that correspond to the ν(NO) stretching vibrations of nitrogen dioxide (NO_2). This NO_2 comes from the nitrate ions (NO_3^-), from the $Ni(NO_3)_2 \cdot 6H_2O$ used as reactant, that have been occluded within the nickel hydroxide structure during synthesis. Despite the difference in the interlaminar distance, the mass loss associated with these NO_3^- ions is equal in both powders suggesting that these ions are the responsible of the hydrotalcite-like structure, rather than the brucite-like one, that is instantaneously generated by the oversaturation of the ammonia solution. On the one hand, for ANHUS-1, with and interlaminar distance of 6.6 Å determined by HRTEM, a mass loss due to water molecules of around 7 % was observed in the TGA plot. On the other hand, an increase of approximately 48 % of the interlaminar distance (from 6.6 Å in sample ANHUS-1 to 9.9 Å in sample ANHSC) allows the incorporation of an extra 42 % of water (from 7 % in sample ANHUS-1 to 10 % in sample ANHSC), which corroborates the different hydration degree of both powders. Consequently, once the alpha structure is generated the water content can be related to the interlaminar distance. Sonication promotes the evacuation of water molecules within the interlaminar space, constraining the interlaminar distance and therefore, tuning this crystallographic parameter.

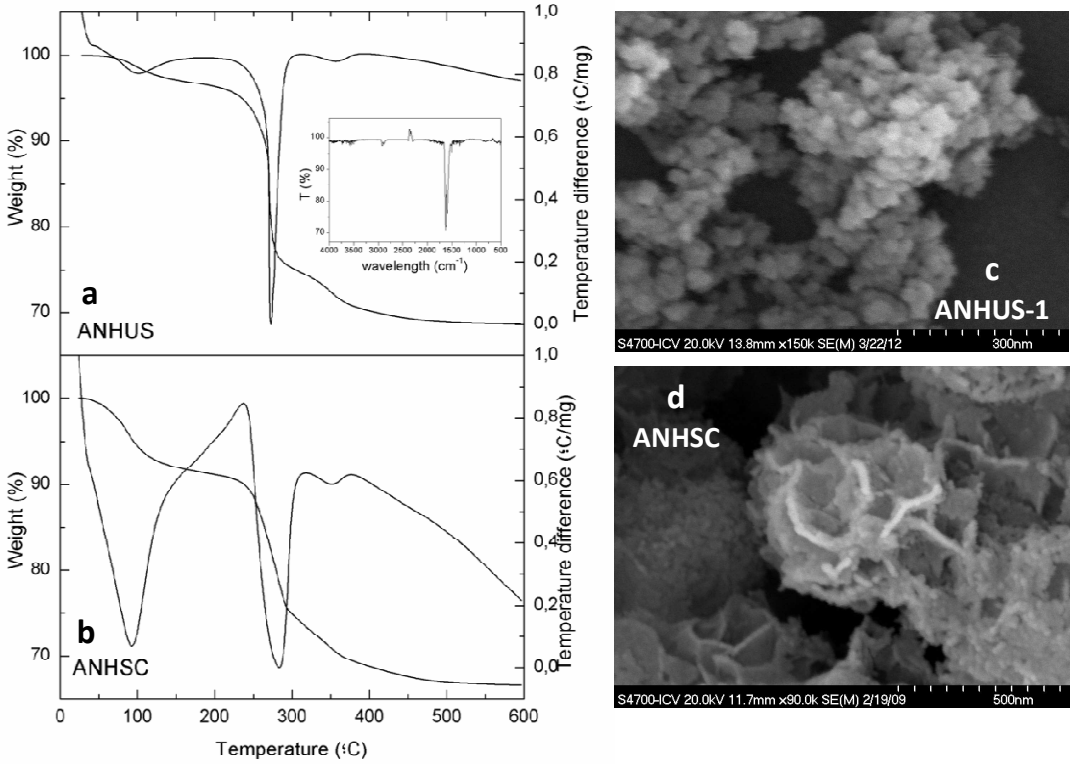

Fig. 8. a and b) DSC-TGA curves of samples ANHUS-1 and ANHSC, respectively and FTIR spectrum of gases generated at 350ºC during DSC-TGA experiments for sample ANHUS (inset graph) and, c and d) SEM images of samples ANHUS-1 and ANHSC, respectively, after calcination at 450°C in air.

SEM images in figure 8c and 8d show the feature of NiO powder obtained after thermal treatment of ANHUS-1 and ANHSC powders in air at 450°C. Unexpectedly, the thermal treatment in the flower-like ANHUS-1 powders forces the disaggregation of 3D nanostructure into single nanoparticles (NPs) of 20-30 nm in diameter (fig. 10c). In figure 8d, the SEM micrograph shows the morphology of a flower-like structure shaped by NPs of 20 nm which strongly resemble the α-$Ni(OH)_2$ arrangements shown in Figure 2f, suggesting that the thermal and ultrasonic activation have a similar effect over the aggregation of the 3D nanostructure. Both thermal and ultrasonic activation verify that the 2D nanostructures (or nanopetals) of the α-$Ni(OH)_2$ are built by NPs.

The α-Ni(OH)$_2$ Nanoflowers and NiO NPs synthetized by sonocrystallization.

Different flower-like structures of α-$Ni(OH)_2$, synthesized by sonication, reverse micelle/microemulsion [14] and microwave [15,37], have been described in the literature. The few papers devoted to these synthesis showed 3D flower-like structures with particle sizes bigger than 1 μm that are composed of 20 nm thick nanopetals with crystallites sizes of 12 and 2-3 nm (for sonication and microwave assisted synthesis, respectively) and nanowires with 20-30 nm in diameter (for the reverse micelle/microemulsion one). However, in our case, spherical nanoflowers with smaller particle sizes and irregular surfaces are obtained with and without ultrasound, being those for powders ANHUS-1 and ANHUS-5 around 200 nm and 400 nm in diameter, respectively, and considerably smaller than the dimension of the ANHSC structure.

The precipitation method followed in our experiments, i. e. the oversaturation of the basic ammonia solution with the nickel source, generates a high rate of nucleation followed by the subsequent growth of formed nuclei and later aggregation. Although the quickness of the synthesis method doesn't allow to measure the induction time, generally it has been demonstrated for longer synthesis times that the perturbation produced by the ultrasound decreases this parameter, as well as the metastable zone, thereby affecting the nucleation process [32]. For all powders (in silence conditions or under the effect of ultrasound) a diffusive mechanism governs particle growth in the (00l) direction. The high nuclei density favors the diffusive mechanism and the bigger seeds grow at expenses of the smaller ones following an Ostwald ripening model and resulting in the initial 2D nanostructures. The oversaturated media and the quickness of the process, forces the nuclei and the growing particles to be incorporated into the already existing ones, therefore creating the 3D nanostructures. Previous results on the synthesis of β-$Ni(OH)_2$ have demonstrated that it is possible to avoid the 3D nanostructures by specifically capping certain planes of the growing structures by using polyelectrolytes [38]. This way, the particles are forced to grow only in 2D. However, in the absence of such capping agents, as is the case of this study, the particles are free to grow into 3D structures creating the flower-like morphologies.

The main morphological difference between the ANHSC and ANHUS flower-like powders is the size of the 3D structures, while HRTEM inspection reveals the apparition of nano-domains within the "petal" nanostructure (figures 5 and 6) when ultrasound is employed. The crystallography of the powders also changes due to the use of ultrasound in terms of planes distance and crystal size due to the amount of water allocated within the structure and the spatial confinement, respectively. These crystallographic differences are associated to a drastic increase in structural defects, such as stacking and crystal alignment faults, created by the acoustic cavitation. If we consider that the powders were prepared using the same reactants

and that the unique difference between them is the presence of ultrasound, results suggest that the ultrasound affects the synthesis of α-$Ni(OH)_2$ at three different levels of organization, as proposed in the scheme of figure 9: i) nuclei precipitation (0D) due to oversaturation conditions, ii) nuclei aggregation to form nanocrystal and therefore the 2D nanostructures (in the case of ANHSC, nuclei tend to organize to minimize their energy while in the case of ANHUS, the ultrasound creates a strong disruption which forces the nuclei to randomly orientate within the planar structures), and iii) diffusion and growth of the 3D flower-like morphologies.

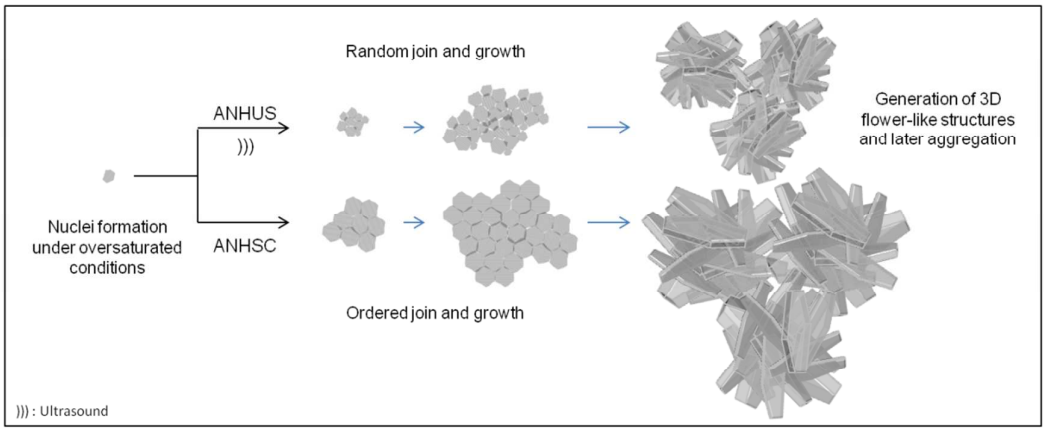

Fig. 9. Scheme of the formation of 3D flower-like structures.

As discussed above, the shockwaves created by the ultrasound in the liquid facilitate the formation of a larger number of dispersed seeds leading to a random crystal growth and further aggregated structures. Consequently the immediate effect of the acoustic waves is the dispersion of nuclei leading to a higher population with smaller and narrower particle sizes. The dispersion effects and its consequent reduction on the Ostwald ripening mechanism result in small crystallites (2.2-2.4 nm in table 1) as well as small 3D structures (200-400 nm in table 2). Despite the difference in crystal and 3D particle sizes between powders, the ratio particle/crystallite size determined for ANHUS-1 and ANHUS-5 are the smallest ever reported. This parameter has been related in the literature with the electrochemical performance of the α-$Ni(OH)_2$ [12], proving that for smaller particle/crystallite ratios the appearance of stacking faults results in an increased electrochemical capacity of the α-$Ni(OH)_2$ that meets the requirements for battery electrode applications.

The effectiveness of $Ni(OH)_2$ or NiO in devices for energy storage (batteries or supercapacitors) [18] and generation (photocathodes) [39], largely depends on the crystallite size and morphology of the active material. The flower-like morphology could increases the electro and photochemical response of this material due to the ultrathin walls of the 2D nanopetal structure and the higher specific surface area than can be achieve with this kind of structures [24], but also the material response can be attributed to the quantum confinement in nanosized particles and chemical defects and vacancies on the lattice. In this sense, Figure 10 a and b shows, respectively, the UV-vis spectrum of ANHUS-1 and ANHUS-5 and corresponding oxides (ANOUS-1 and ANOUS-5) measured at room temperature in the wavelength range between 200-800 nm. Similar adsorption bands can be observed. The first one, at around 250 nm, can be attributed to the bandgap absorption which is more intense in the case of NiO. The other bands that appear at approximately 390 and 675 nm in the UV-vis spectra, especially for α-$Ni(OH)_2$, correspond to two different ligand field bands assigned to the $^3A_{2g}(F) \rightarrow {}^3T^{1g}(P)$ and $^3A_{2g}(F) \rightarrow {}^3T^{1g}(F)$ transitions. The small shoulder at 750 nm can be attributed to the spin forbidden $^3A_{2g}(F) \rightarrow {}^3E_g(G)$ transition [40].

The optical bandgap absorption energy can be calculated using the following formula:

$$\alpha = \frac{A(E_g - h\nu)^n}{h\nu}$$

where α is the absorption coefficient, A is a constant, E_g is the bandgap energy and n is a number equal to 0.5 for a direct bandgap and 2 for an indirect one [41,42]. Graphically it can be estimated extrapolating to zero absorption (α=0) in the linear part of the curve $(\alpha h\nu)^{1/n}$ vs photon energy (hν). These curves are shown at the insets in figure 10 a and b. In the case of ANHUS-1 and ANHUS-5 bandgaps are 4.16 eV and 4.45 eV, respectively, while the bandgap of the oxides decreases down to 3.11 eV for ANOUS-1 and 3.26 eV for ANOUS-5.

The optical bandgap of α-$Ni(OH)_2$ powders is reported for the first time in the literature, since all the data found up to date corresponds to the β-$Ni(OH)_2$ (3.6-3.9 eV) or NiO. Based on their band gap values, α-$Ni(OH)_2$ powders synthesized under ultrasound results in a promising material for its use as electrochemical capacitor [12]. On the other hand, the accepted value for the band gap of bulk NiO is 4.3 eV [43], while further decrease in crystalline size results in blue shifting of the absorption spectra (e.g., size quantization effect) [44]. However, results plotted in figure 10b show low values of band gap for NiO. A plausible explanation for this change in band gap with respect to the size is that the defects induce delocalization of molecular orbitals in the conduction band edge (e.g., LUMO) and create shallow/deep traps in electronic energy,

in turn causing the red-shift of the absorption spectra [45]. The band gap determined for ANOUS powders are among the lower values reported in the literature, as a consequence of the crystallographic distortions created by the ultrasound waves at the ANHUS synthesis. In fact, the high absorbance of the NiO (ANOUS-1 and ANOUS-5) is due to the heavy black color of the powder that should be originated from the nickel vacancies in the NiO nanocrystals [46]. This defect is responsible for the p-type semi-conductivity of this material, and then the low band gap of those NPs could promote their use as photoactive material.

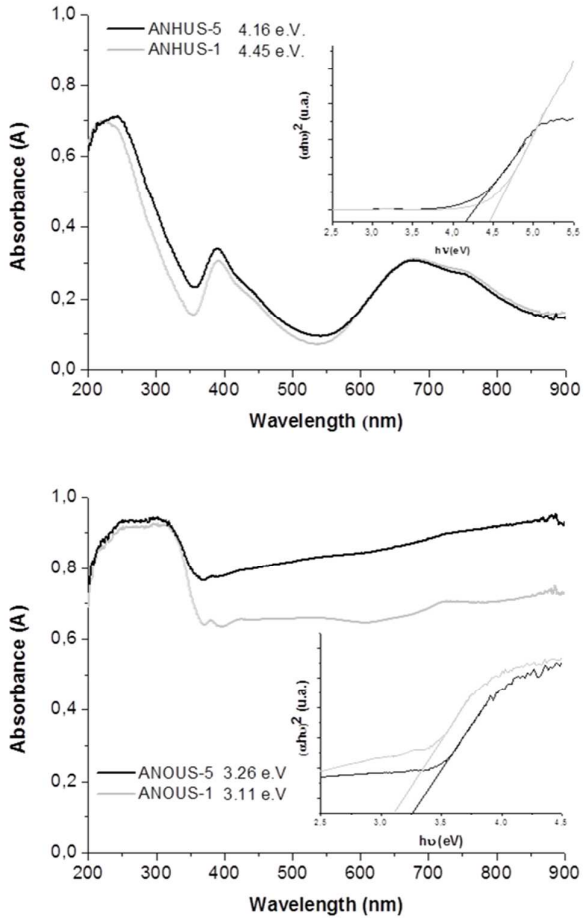

Figure 10. UV–vis spectra and band gap energy of α-$Ni(OH)_2$ (a) and NiO (b) synthesized under 1500 W/cm^2 mol (ANHUS-5 and ANOUS-5) and 4000 W/cm^2 mol (ANHUS-1 and ANOUS-1).

Conclusions:

The conditions for the instantaneous precipitation of the pure turbostratic polymorph α-$Ni(OH)_2$ was described. The product of the instantaneous synthesis is a 3D flower-like nanostructure whose "petals" have a thickness ranging 10-20 nm. The application of adequate power of sonication to the volume of precursors promotes the separation of nucleation and growth processes leading to the precipitation of disperse and single 3D nanostructures with mean sizes in number raging 190-530 nm. The size of synthetic powders depends on the sonication power, this way, the stronger the ultrasound power, the smaller are the 3D entities which precipitate instantaneously.

For the quantification of the effectiveness of sonication, the S parameter has been proposed, which is equivalent to the number of watts per cm^2 that a mol of $[Ni(NH_3)_6]^{2+}$ experiences. In order to produce flower-like nanostructures smaller than 1 μm, the S parameter should be higher as the power of the sonication increases, i.e. for 45 W/cm^2 the S parameter should be higher than 1500 W/cm^2mol while when 80 W/cm^2 is applied the S parameter should be more than double achieving 4000 W/cm^2mol.

Sonication has a strong effect at all levels of structural and crystallographic ordering. The evaluation of the porosity in the 3D nanostructures evidences the growth differentiation when ultrasound is applied. Microporosity (< 2 nm) in flower-like 3D nanostructures is not so relevant as meso and macroporosity, but it follows an increasing trend with the S parameter. Moreover, the similitude in the fine mesopores distribution of α-$Ni(OH)_2$ nanostructures (2-3 nm) obtained under silence and mild sonication conditions, if compare with particles obtained under a high ultrasound power (3-10 nm), identifies the effect of the mechanical disruption in the staking of the turbostractic units when α-Ni(OH)2 nuclei grow. Moreover, the narrower and lower population of large mesopores and fine macropores (20-60 nm) in the particles synthesized under mild sonication evidences the presence of a half built and less intricate tridimensional nanostructure, than individual flower-like nanostructures obtained under a stronger sonication, where meso-macroporosity achieved 100 nm.

Related to the crystallographic order, the crystal size and the interlaminar distance decrease when ultrasound is applied. Sonication alters the crystal orientation when 2D nano-aggregates grow shaping nanopetal arrays in a 3D configuration. Changes on the orientation of crystal growth promote a spatial confinement leading to smaller crystal domains and extremely low crystallite sizes (2.2-2.4 nm). That leads to the lowest ratio particle/crystallite size reported up to day in the literature. On the other hand, the interlaminar distance is smaller when the

crystal grows under the influence of ultrasound (7.1-7.5 Å). Comparing the thermal behavior of synthetic powders and their crystallography, results show that the interlaminar distance depends on the amount of water allocated within the flower-like nanostructure, increasing from 7% to 10% with the ultrasound application. Hence, it can be concluded that the higher is the sonication power the larger is the amount of water occluded and, therefore the interlaminar distance of sonicated flower-like particles.

Results evidences that α-$Ni(OH)_2$ grows confined in disordered nanodomains which aggregates forming 2D nanopetals which arranges in 3D flower-like nanostructures. Crystallographic confinement and disorder are the cause of the formation of NiO nanoparticles, lower than 30 nm in size, after the calcination of α-$Ni(OH)_2$ powders. The band gap of α-$Ni(OH)_2$ has been reported for the first time in the literature. Individual flower-like 3D structures of α-$Ni(OH)_2$ synthesized under ultrasound exhibits a wide band gap (4.2-4.5 eV), in the range of bulk NiO (4.23 eV) and higher than values measured for the stable allotropic phase, β-$Ni(OH)_2$ (3.6-3.9 eV). Morphological and crystallographic characteristics of the synthesized α-$Ni(OH)_2$ meet the necessary features of the electrochemical capacitors. NiO NPs obtained by calcination of the α-$Ni(OH)_2$ exhibits extremely low band gap values, 3.11-3.26 eV, due to the presence of vacancies and crystallite defaults, highlighting the appropriateness use of this NPs in photocathodes.

Experimental Section

Nickel nitrate hexahydrated ($Ni(NO_3)_2{\cdot}6H_2O$; purity 99.9%, Panreac Química S.A.U., Spain) and ammonium hydroxide (33% Panreac Química S.A.U., Spain) were used as reactants. Predominant species diagram were created by using the MEDUSA software and the hydrochemical equilibrium-constant database (HYDRA) [47].

High intensity ultrasonic horn (Ti horn, 24 kHz, 100 W/cm^2, UP 400s, Dr. Hielsecher, Germany) was use as ultrasound source. Solutions were prepared by adding an appropriate amount of solid $Ni(NO_3)_2{\cdot}6H_2O$ ($[Ni^{2+}]_{solution}$= 0.65 M) powders to a 2 M ammonium hydroxide solution. Formation of a green powder was observed immediately (silence conditions, sample ANHSC). A similar process was performed under the influence of ultrasound into the solution that was kept for 1 minute (samples ANHUS). All powders were then filtrated and dried at 60ºC/2h for further characterization. The influence of different variables (such as ultrasonic radiation intensity, volume and concentration) in the interlaminar distance and crystallite size of the

obtained powders have been studied. All powders obtained were filtered using polymeric filters (ø = 0.22 µm), washed with distilled water at pH ~ 10 (adjusted with tetramethyl ammonium hydroxide) for several times and then dried at 60 ºC for 2 h.

Specific surface area was measured on the green powders with a Monosorb Surface Area MS-13 equipment (Quantachrome Corporation, USA)). N_2 adsorption/desorption measurements were carried out with a Micromeritics ASAP 2020 (USA). Density was calculated by helium pycnometry using a Monosorb Multipycnometer (Quantachrome Corporation (USA)). BET diameter was calculated using the equation $D_{BET} = 6/(SSA \cdot \rho)$, where SSA is the specific surface area and ρ is the density of the powder.

Crystallographic phases were identified by XRD analysis performed with a Siemens D5000 diffractometer (Germany) with a Kristalloflex 710 generator (Kα(Cu) λ = 1.5405 Å; 40 KV; 30 mA; 2θ = 5-70). Differential scanning calorimetric analysis (DSC) and thermogravimetric analysis (TGA) were carried out with a SDT Q600 analyzer (5 ºC/min, T = 25-600ºC, N_2 atmosphere, TA instruments). Coupled to the gases exhaust fume there is a FTIR analyzer (Thermo Scientific Nicolet 6700 FT-IR Spectrometer) that allows the identification of gases generated during the heating processes in DSC-TGA experiments. The morphology of the powders was examined by FE-SEM (Hitachi S-4700, Japan) and TEM (Hitachi H-7100, Japan). High resolution TEM images were recorded using a Jeol JEM 2100 electron microscope operating at 200 kV and equipped with an Orius Gatan CCD Camera. To avoid degradation of the hydroxides, TEM images were recorded under low energy conditions.

Zeta potential measurements were carried out in a Zetasizer Nano ZS (Malvern Instruments Ltd., UK) (for nickel hydroxide powders). Colloidal suspension for zeta potential measurements were prepared in KCl 10^{-2} M in order to maintain constant the ionic strength of the medium and with solid contents of 0.1 g/L. Tetramethylammonium hydroxide (TMAH) was used to adjust the pH. Particle size measurements were performed using the same equipment (Zetasizer Nano ZS, Malvern Instruments Ltd., UK).

Acknowledgements:

This work has been supported by MINECO-Spain under contract MITICO, MAT2012-38650-C02-02, and by the Madrid Autonomic Community under contract MULTIMAT Challenges, S2013/MIT-2862. Dr. Gonzalez acknowledges the MINECO-Spain Torres Quevedo funding.

Keywords: alpha nickel hydroxide • 3D nanostructured particles • spatial confinement • crystallographic structure.

References:

1. A. S. Aricò, P. Bruce, B. Scrosati, J.-M. Tarascon, and W. van Schalkwijk, *Nat. Mater.*, 2005, **4**, 366–377.
2. J. Maier, *Nat. Mater.*, 2005, **4**, 805–815.
3. J. N. Tiwari, R. N. Tiwari, and K. S. Kim, *Prog. Mater. Sci.*, 2012, **57**, 724–803.
4. J. Ning, X. Xu, C. Liu, and D. L. Fan, *J. Mater. Chem. A*, 2014, **2**, 15768–15773.
5. X. Liu and L. Yu, *J. Power Sources*, 2004, **128**, 326–330.
6. X. Han, X. Xie, C. Xu, D. Zhou, and Y. Ma, *Opt. Mater. (Amst).*, 2003, **23**, 465–470.
7. S. Cabanas-Polo, R. Bermejo, B. Ferrari, and A. J. Sanchez-Herencia, *Corros. Sci.*, 2012, **55**, 172–179.
8. Z. Liang, Y. Zhu, and X. Hu, *J. Phys. Chem. B*, 2004, **108**, 3488–3491.
9. X. Sun, G. Wang, J.-Y. Hwang, and J. Lian, *J. Mater. Chem.*, 2011, **21**, 16581–16588.
10. H. Wang, J. Gao, Z. Li, Y. Ge, K. Kan, and K. Shi, *CrystEngComm*, 2012, **14**, 6843.
11. M. Aghazadeh, A. N. Golikand, and M. Ghaemi, *Int. J. Hydrogen Energy*, 2011, **36**, 8674–8679.
12. M. Casas-Cabanas, J. Rodriguez-Carvajal, J. Canales-Vazquez, and M. R. Palacin, *J. Mater. Chem.*, 2006, **16**, 2925–2939.
13. D. Yang, R. Wang, M. He, J. Zhang, and Z. Liu, *J. Phys. Chem. B*, 2005, **109**, 7654–7658.
14. M. Cao, X. He, J. Chen, and C. Hu, *Cryst. Growth Des.*, 2007, **7**, 170–174.
15. M. Y. Cheng and B. J. Hwang, *J. Colloid Interface Sci.*, 2009, **337**, 265–271.
16. L. Gong, X. Liu, and L. Su, *J. Inorg. Organomet. Polym. Mater.*, 2011, **21**, 866–870.
17. H. Wang, H. S. Casalongue, Y. Liang, and H. Dai, *J. Am. Chem. Soc.*, 2010, **132**, 7472–7477.
18. H. Jiang, T. Zhao, C. Li, and J. Ma, *J. Mater. Chem.*, 2011, **21**, 3818–3823.
19. G. Zhang, X. Zhao, and L. Zhao, *Mater. Lett.*, 2012, **66**, 267–269.
20. S. M. Zhang and H. C. Zeng, *Chem. Mater.*, 2009, **21**, 871–883.
21. P. Jeevanandam, Y. Koltypin, and A. Gedanken, *Nano Lett.*, 2001, **1**, 263–266.

22. S. Cabanas-Polo, B. Ferrari, and A. J. Sanchez-Herencia, *Bol. la Soc. Esp. Ceram. y Vidr.*, 2014, **53**, 265–274.

23. C. Nethravathi, B. Viswanath, M. Sebastian, and M. Rajamathi, *J. Colloid Interface Sci.*, 2010, **345**, 109–115.

24. L. Xu, Y. Ding, C. Chen, L. Zhao, C. Rimkus, R. Joesten, and S. L. Suib, 2008, 308–316.

25. A. Delahaye-Vidal and M. Fligarz, *J. Appl. Electrochem.*, 1987, **17**, 589–599.

26. M. Rajamathi and P. V. Kamath, *Mater. Lett.*, 2003, **57**, 2390–2394.

27. M. Vidotti, R. P. Salvador, and S. I. Córdoba de Torresi, *Ultrason. Sonochem.*, 2009, **16**, 35–40.

28. C. Liu and Y. Li, *J. Alloys Compd.*, 2009, **478**, 415–418.

29. S. Cabanas-Polo, K. S. Suslick, and a J. Sanchez-Herencia, *Ultrason. Sonochem.*, 2011, **18**, 901–906.

30. E. Revalor, Z. Hammadi, J. P. Astier, R. Grossier, E. Garcia, C. Hoff, K. Furuta, T. Okustu, R. Morin, and S. Veesler, *J. Cryst. Growth*, 2010, **312**, 939–946.

31. M. D. Luque de Castro and F. Priego-Capote, *Ultrason. Sonochem.*, 2007, **14**, 717–724.

32. J. Dodds, F. Espitalier, O. Louisnard, R. Grossier, R. David, M. Hassoun, F. Baillon, C. Gatumel, and N. Lyczko, *Part. Part. Syst. Charact.*, 2007, **24**, 18–28.

33. M. Meyer, A. Bée, D. Talbot, V. Cabuil, J. M. Boyer, B. Répetti, and R. Garrigos, *J. Colloid Interface Sci.*, 2004, **277**, 309–315.

34. L. Zhu, B. H. Calhoun, Q. Ge, R. P. Quirk, S. Z. D. Cheng, E. L. Thomas, B. S. Hsiao, F. Yeh, L. Liu, and B. Lotz, *Macromolecules*, 2001, **34**, 1244–1251.

35. T. M. Chung, T. C. Wang, R. M. Ho, Y. S. Sun, and B. T. Ko, *Macromolecules*, 2010, **43**, 6237–6240.

36. M. A. Kiani, M. F. Mousavi, and S. Ghasemi, *J. Power Sources*, 2010, **195**, 5794–5800.

37. S. Ran, Y. Zhu, H. Huang, B. Liang, J. Xu, B. Liu, J. Zhang, Z. Xie, Z. Wang, J. Ye, D. Chen, and G. Shen, *CrystEngComm*, 2012, **14**, 3063.

38. S. Cabanas-Polo, K. S. Suslick, and A. J. Sanchez-Herencia, *Ultrason. Sonochem.*, 2011, **18**, 901–906.

39. I. Barceló, E. Guillén, T. Lana-Villarreal, and R. Gómez, *J. Phys. Chem. C*, 2013, **117**, 22509–22517.

40. M. A. Rocha, H. Winnischofer, K. Araki, F. J. Anaissi, and H. E. Toma, *J. Nanosci. Nanotechnol.*, 2011, **11**, 3985–3996.

41. S. B. Kulkarni, V. S. Jamadade, D. S. Dhawale, and C. D. Lokhande, *Appl. Surf. Sci.*, 2009, **255**, 8390–8394.

42. L. Kumari and W. Z. Li, *Phys. E Low-Dimensional Syst. Nanostructures*, 2009, **41**, 1289–1292.

43. G. A. Sawatzky and J. W. Allen, *Phys. Rev. Lett.*, 1984, **53**, 2339–2342.

44. S. Thota, J. H. Shim, and M. S. Seehra, *J. Appl. Phys.*, 2013, **114**, 214307.

45. H. Lin, C. P. Huang, W. Li, C. Ni, S. I. Shah, and Y. H. Tseng, *Appl. Catal. B Environ.*, 2006, **68**, 1–11.

46. E. W. McFarland and H. Metiu, *Chem. Rev.*, 2013, **113**, 4391–4427.

47. I. Puigdomenech, *K. R. I. o. T. Dep. Chem.*

Caption to figures

Fig. 1. XRD plots of samples prepare under different conditions (shown in table 1). All peaks correspond to α-$Ni(OH)_2$ except the ones pointed with (•) in sample ANHUS-6 that correspond to β-$Ni(OH)_2$.

Figure 2. FESEM images of a) sample ANHSC where a spongy 3D flower-like structure with wall thickness <20 nm can be observed, b) ANHUS-6, c) ANHUS-5, d)ANHUS-3, e) ANHUS-2 and f) ANHUS-1.

Figure 3. (a) Adsorption-desorption isotherms of N_2 and the partial volume of each pore diameter measured for ANHSC, ANHUS-1 and ANHUS-5. Micrographs of the petal structure of the ANHUS-1 (b) and ANHUS-5 (c) powders.

Figure 4. Particle size distribution of samples ANHUS-1 and ANHUS-5 at the post-reaction conditions in number (a) and volume (b).

Figure 5. TEM (a and b) and HRTEM (c and d) images of samples ANHUS-1 (a and c) and ANHSC (b and d).

Figure 6. HRTEM images of sample a) ANHUS, b) ANHSC (where the different crystallite sizes can be observed) and c) NiO, derived from the transformation of $Ni(OH)_2$ due to the analysis conditions. After transforming to NiO, crystallographic distances along the (101) plane of NiO can be observed (inset figures in figure 6c).

Figure 7. (a) XRD pattern of samples ANHUS-1 (upper) and ANHSC (lower). Both samples were identified as the α-$Ni(OH)_2$ using the JCPDS card 22-0444. (b) HRTEM image of sample ANHUS-1 showing stacking faults along the 001 plane. (c) HRTEM micrographs of ANHUS-1 with its corresponding IFFT. (d) HRTEM micrographs of ANHSC with its corresponding IFFT.

Fig. 8. a and b, DSC-TGA curves of samples ANHUS-1 and ANHSC, respectively and FTIR spectrum of gases generated at 350ºC during DSC-TGA experiments for sample ANHUS (inset graph), c and d, SEM images of samples ANHUS-1 and ANHSC, respectively, after calcination at 450ºC in air.

Fig. 9. Scheme of the formation of 3D flower-like structures.

Figure 10. UV–vis spectra and band gap energy of α-$Ni(OH)_2$ (a) and NiO (b) synthesized under 1500 W/cm^2 mol (ANHUS-5 and ANOUS-5) and 4000 W/cm^2 mol (ANHUS-1 and ANOUS-1).